Energy harvesting from ultra-low frequency vibrations through a quasi-zero stiffness electromagnetic energy harvester

Wei Wang^{1, 2*}, Ying Zhang³, Chris R. Bowen⁴, Zon-Han Wei^{1, 2,*}, Junyi Cao³

- Nano Opto-mechatronics and Biomedical Engineering Laboratory, School of Mechanics and Safety Engineering, Zhengzhou University, Zhengzhou, 450001, China
- 2. Institute of Intelligent Sensing, Zhengzhou University, Zhengzhou 450001, China
- 3. Key Laboratory of Education Ministry for Modern Design and Rotor-Bearing System, School of Mechanical Engineering, Xi'an Jiaotong University, Xi'an, 710049, China
- 4. Materials and Structures Centre, Department of Mechanical Engineering, University of Bath, Bath BA27AY, UK

Abstract

To scavenge vibrational energy from ultra-low frequency vibrations with low excitation levels, this paper presents a novel quasi-zero stiffness electromagnetic energy harvester (QZS-EMEH) by exploiting a rolling magnet system. By calculating the nonlinear restoring force exerted on the moving magnet, the parameter region that results in conditions of quasi-zero stiffness is determined, and a theoretical model of the QZS-EMEH is established. Based on the method of harmonic balance, the analytical solution of the QZS-EMEH is derived, and the influence of system parameters on the response characteristics and energy harvesting performance is discussed. Numerical and theoretical

^{*}Correspondence: w_wei2013@zzu.edu.cn (W. Wang), profwei@zzu.edu.cn (Z.H. Wei)

results indicate that the QZS-EMEH can efficiently harness energy in a wide frequency range under

low-level excitations. Furthermore, the nonlinear dynamics of the QZS-EMEH are investigated

based on the bifurcation diagram, phase orbit, Poincaré map, and basin of attraction, demonstrating

that appropriate initial conditions can lead to the high-energy orbit oscillation. Finally, realistic

ambient vibration accelerations from a bus and a human body are applied to excite the QZS-EMEH,

and the results illustrate that the QZS-EMEH can generate considerable electrical output power and

has excellent application prospects.

Keywords: Energy harvesting; electromagnetic; quasi-zero stiffness; rolling magnet; ultra-low

frequency

2

1. Introduction

Recently, the rapid development of the technology of communication and microelectronics has witnessed the widespread adoption of low-power consumption wireless sensors and portable electronics[1]. These devices are typically powered by conventional battery technologies which require regular replacement or recharging to sustain the steady power demand of devices[2]. The technology of *vibrational energy harvesting*, which aims to convert ambient vibrational energy into useful electrical energy, has been viewed as a promising strategy to supply electricity for low-power consumption devices[3]. Currently, there are three typical energy conversion mechanisms applied to scavenge vibrational and mechanical kinetic energy, namely the *piezoelectric*[4], *electromagnetic*[5], and *electrostatic*[6] effects. Among them, electromagnetic energy harvesters (EMEHs) have been considered as a promising method to harness vibrational energy due to their small internal impedance and large output current[7]. Previously, a variety of EMEHs have been designed and optimized based on linear resonance mechanisms[8, 9]. However, linear EMEHs only perform well at their resonance frequencies and a small change in the vibration frequency can therefore greatly degrade the energy harvesting performance[10].

To overcome the narrow band issues of linear EMEHs, a number of nonlinear EMEHs based on mechanical and nonlinear mechanisms have been proposed and investigated numerically, theoretically, and experimentally to harness energy in a wide frequency range and improve output performance[11]. By utilizing the structure of the cantilever beam, Barton et al.[12] presented a nonlinear EMEH through a particular arrangement of magnets in conjunction with an iron-cored stator; their experimental data indicated that the response frequency range was broadened. By modifying the multi-stable structure proposed by Zhou et al.[13], Deng and Wang[14] proposed a

multi-stable EMEH where the external magnets were positioned along a concave surface that was parallel to the motion trajectory of the cantilever tip. Experimental results demonstrated that a significant broadband response was obtained with a maximum RMS power output of 40.2 mW at an excitation of 0.45g. Liu et al.[15] proposed a nonlinear wideband EMEH by clamping a cantilever beam generator with a curved fixture and their experiments demonstrated that the proposed mechanism could effectively extend the operational bandwidth and provide high power performance. More recently, Foong et al.[16] introduced an anti-phase motion between the coil and the magnets at resonance to enhance the performance of a cantilever beam-based electromagnetic harvester, and experiments indicated that the proposed method led to a great increase in power compared to the conventional method. Furthermore, Foong et al.[17] presented several considerations to be made when optimizing the structural aspects of a single-degree-of-freedom electromagnetic harvester.

An alternative type of EMEH that has attracted significant attention has been based on magnetic-spring configurations, in which an arrangement of magnets led to moving magnets experiencing a repulsive force with respect to the fixed magnets. For the configurations applied in vertical conditions, the structures with only a bottom fixed magnet were preferred. As an example, Zhang et al.[18] proposed a hand-held EMEH that was composed of a magnet array that was aligned to a coil array, and was suspended by a magnetic spring with a bottom magnet. Theoretical analysis was undertaken to explore the performance under the influence of vibrations with low frequency and large amplitude; the experimental results determined under human motion excitation demonstrated the potential application prospect. For an EMEH consisting of one or more spaced magnets that were suspended by a bottom fixed magnet, Struwig et al.[19] developed an electrical and mechanical model and optimized the parameters such as the number of coils, coil height, coil spacing, and the

number of magnets. Under vertical excitation with large levels and horizontal excitation, the moving magnets in magnetic-spring-based EMEHs containing only a bottom magnet will be out of range and the structure will fail to scavenge energy.

To address this challenge, a larger number of magnetic-spring-based configurations with symmetrically fixed magnets have attracted attention. In 2008, Saha et al.[20] reported on a magnetic-spring-based EMEH which levitated a moving magnet using two fixed magnets; the performance of the system under human motion excitation during walking and slow running was evaluated. Mann et al.[21] developed the governing equations of the system concerning the mechanical and electrical domains, and their theoretical and experimental investigations indicated that the presence of nonlinear phenomena improved the effectiveness of the EMEH. Based on a similar configuration, Wang et al.[22] optimized the moving magnetic stack and investigated the output performance of the EMEH under human motion excitation. Masoumi and Wang[23] provided a parametric, numerical, and experimental investigation into a repulsive electromagnetic harvester with a specific arrangement of stacked magnets, which was able to produce a large magnetic field compared to attractive magnetic counterparts. To harness the vibrational energy in a wider frequency range, Mann and Owens[24] developed a bistable EMEH by arranging four magnets around the midpoint of the tube in the device in Ref. [21]. The theoretical and experimental results indicated that the potential well escape phenomenon can be applied to broaden the response frequency range. Nguyen et al.[25] developed analytical models describing the interaction between the magnets and conducted a comparative study between both monostable and bistable systems. They concluded that the application of thin peripheral magnets around the tube led the bistable harvester to move towards monostability. In addition, Gao et al.[26] illustrated a multistable EMEH by arranging additional magnets around the tube with magnetic levitation oscillation. Tristable and quad-stable configurations were obtained experimentally and analyzed utilizing phase portraits, Poincaré section, largest Lyapunov exponent, and bifurcation diagram.

Although multistable configurations exhibiting complex dynamic behaviors can collect energy in a wider frequency range, the vibration level of the external excitation should be sufficiently large to overcome the local potential barriers to achieving the large-amplitude interwell oscillation. To harvest energy in a very low-frequency region and at a very low excitation level, an EMEH with a flat, or almost flat potential function is preferred. Such a potential function is characterized by a configuration with *quasi-zero stiffness* characteristic, which provides an opportunity to scavenge energy at very low frequencies. Recently, Liu et al.[27] proposed a quasi-zero stiffness device capable of vibration isolation and energy harvesting, and their results demonstrated that the proposed system could achieve a high output power and low operating frequencies. Margielewicz et al.[28] investigated the nonlinear dynamics of a quasi-zero stiffness energy harvesting system and indicated that the harvester had an improved ability to scavenge energy in the low range of values of excitation frequencies. Furthermore, Wang et al.[29] introduced the quasi-zero stiffness mechanism to a triboelectric nanogenerator and found that the generator exhibited excellent performance in the ultralow frequency region.

To harvest energy from ultra-low frequency vibrations with low excitation levels, a novel QZS-EMEH is proposed here by utilizing a rolling magnet system. Due to the small mechanical damping, the rolling magnet system has been applied in the area of energy harvesting. For example, Liu et al.[30] reported on a non-resonant rotational EMEH for scavenging energy from irregular human motion and indicated that the device exhibited outstanding output performance. Kuang et

al.[31, 32] investigated the output performance of a magnetic rolling pendulum EMEH under both base and parametric excitation and showed that the presence of subharmonic resonance could broaden the response bandwidth. Although EMEHs based on rolling magnet systems have been studied theoretically and experimentally, the investigation has not focused on the presence of quasi-zero stiffness characteristics.

Therefore, a novel QZS-EMEH is proposed in this paper based on the rolling magnet system to harvest energy from ultra-low frequency vibrations with low excitation levels. The design approach of the QZS-EMEH is illustrated and the parameter region for quasi-zero stiffness characteristics is examined in detail. The nonlinear dynamics and energy harvesting performance of the QZS-EMEH are analyzed theoretically and numerically under harmonic excitations, and the response under realistic ambient vibrations is also evaluated. The remainder of the paper is organized as follows:

Section 2 illustrates the configuration of the QZS-EMEH and provides the corresponding dynamic model; in Section 3, the harmonic balance method is applied to theoretically analyze the response, and the nonlinear dynamic behavior is highlighted. Furthermore, the vibrational signals from a bus and a human body are applied to excite the QZS-EMEH in Section 4 and the potential application prospect is demonstrated. Finally, conclusions are drawn in Section 5.

2. Description and modeling of the QZS-EMEH

Figure 1 illustrates the schematic diagram of the QZS-EMEH that is based on a rolling magnet system. The system is composed of two coils, a single rectangular magnet (A), and four cylindrical magnets (B, C, D, and E). All magnets have the type of N35 (Magnetization: 8.9×10^5 A/m) and a thickness of 10 mm. In addition, the cylindrical magnets have a radius of 5 mm (r_1). The polarization directions of the magnets are arranged axially so that magnet D is repelled by magnets B, C, and E

and attracted by magnet A. In this configuration, magnets A, B, C, E, and the coils are fixed to the base, while magnet D is free to vibrate. Due to the constraint induced by the magnetic attraction force between magnets A and D, the oscillation of the moving magnet D is rolling on the surface of the magnet A. Magnets B and C are fixed to the edges of the end of magnet A, as shown in Fig. 1 and the distance between them is assumed to be $2d_1$. The repulsive force between magnets B, C, and D keeps the vibration of moving magnet D within a certain range. Furthermore, magnet E is positioned perpendicular to the surface of magnet A. When magnet D is at the position having a distance of d_1 to magnet B, the distance between magnets D and E is represented by d_2 . By adjusting the parameters d_1 and d_2 , the system could exhibit the characteristic of quasi-zero stiffness. When an external excitation is applied to the base, magnet D will roll along the surface of magnet A back and forth due to the repulsive force from magnets B, C, and E. On this occasion, the magnetic flux through the two coils positioned below the track of moving magnet D will change, thus generating an electrical current. To be noted, the above description illustrates the concept of the QZS-EMEH. In realistic application, a proper supporting structure can be designed to fix the magnets and coils.

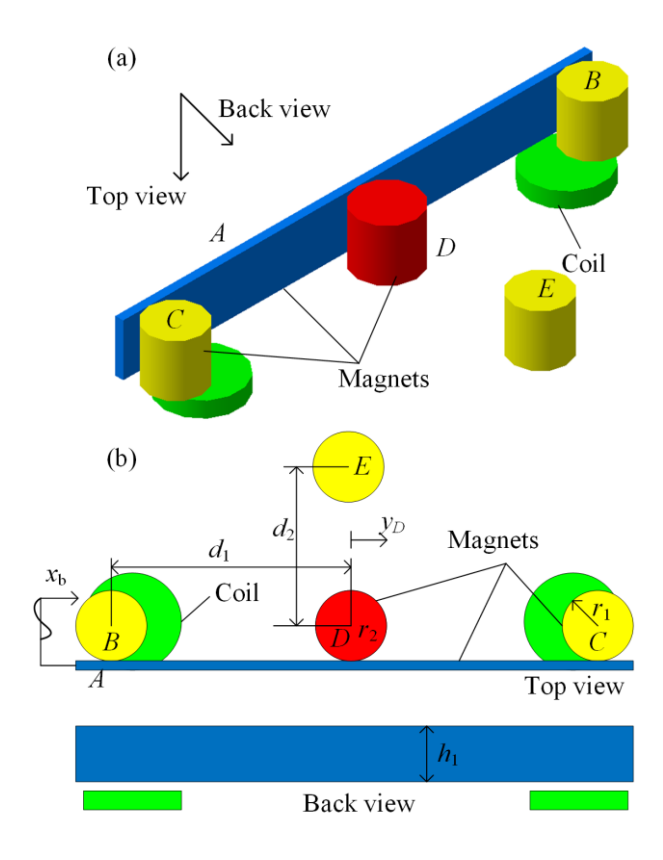


Fig. 1 Schematic diagram of the quasi-zero stiffness electromagnetic energy harvester (QZS-EMEH).

In the configuration described above, the nonlinear oscillation of the moving magnet D is mainly the result of the magnetic force from magnets B, C, and E. The magnetic attractive force between magnets A and D does not affect the characteristic of motion and can be neglected. Therefore, different nonlinear restoring forces exerted on magnet D can be achieved by adjusting the parameters d_1 and d_2 . Due to the same size of magnets B, C, D, and E, the magnetic repulsive force between two cylindrical magnets is calculated and the overall nonlinear restoring force exerted on magnet D is computed according to the geometrical parameters of the configuration. Herein, the Ansys Maxwell software is applied to calculate the magnetic repulsive force between two cylindrical magnets with different distances. The blue circles in Fig. 2 (a) describe the simulation results from Ansoft Maxwell and are fitted with a red line which can be expressed as a polynomial form as shown in Eq. (1).

$$F_m = \sum_{i=0}^n a_n d^i \tag{1}$$

where d is the distance between two cylindrical magnets and a_n is the coefficient of the polynomial. Regarding the configuration with the parameters of d_1 and d_2 , the nonlinear restoring forces exerted on magnet D can be calculated as Eq. (2) when the displacement of the rolling magnet D relative to the base is x ($x=y_D-x_b$). For the convenience of subsequent calculations, the nonlinear restoring force is fitted as a cubic polynomial as in Eq. (3), where k_1 and k_3 are the coefficients of the polynomial.

$$F_{mt} = \sum_{i=0}^{n} a_i \left(d_1 - x \right)^i - \sum_{i=0}^{n} a_i \left(d_1 + x \right)^i - \sum_{i=0}^{n} a_n \frac{x}{\sqrt{d_2^2 + x^2}} \left(\sqrt{d_2^2 + x^2} \right)^i$$
 (2)

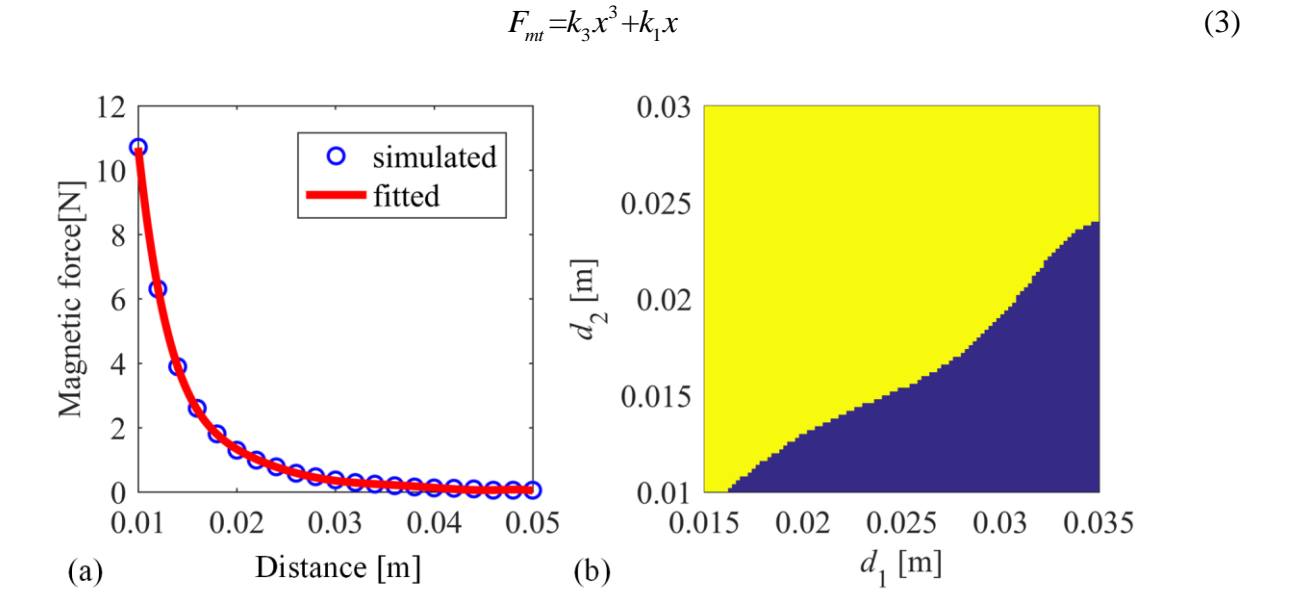


Fig. 2 (a) Magnetic force between two cylindrical magnets with different distances; (b) parameter region: yellow-monostable, blue-bistable.

The potential energy function is a useful tool to analyze the characteristics of nonlinear systems. By integrating the nonlinear restoring force described by Eq. (3) to displacement x, the potential energy function of the system can be achieved. According to the number of stable equilibrium points in the potential energy function, the configuration proposed in this paper can achieve both monostable and bistable systems when with different values of d_1 and d_2 . Fig. 2 (b) illustrates the parameter region of the system in which the yellow data represents the parameters that lead to a

monostable system, while blue data indicates a bistable configuration. By adjusting the parameters of d_1 and d_2 , the QZS-EMEHs can be obtained at the border between the two basins.

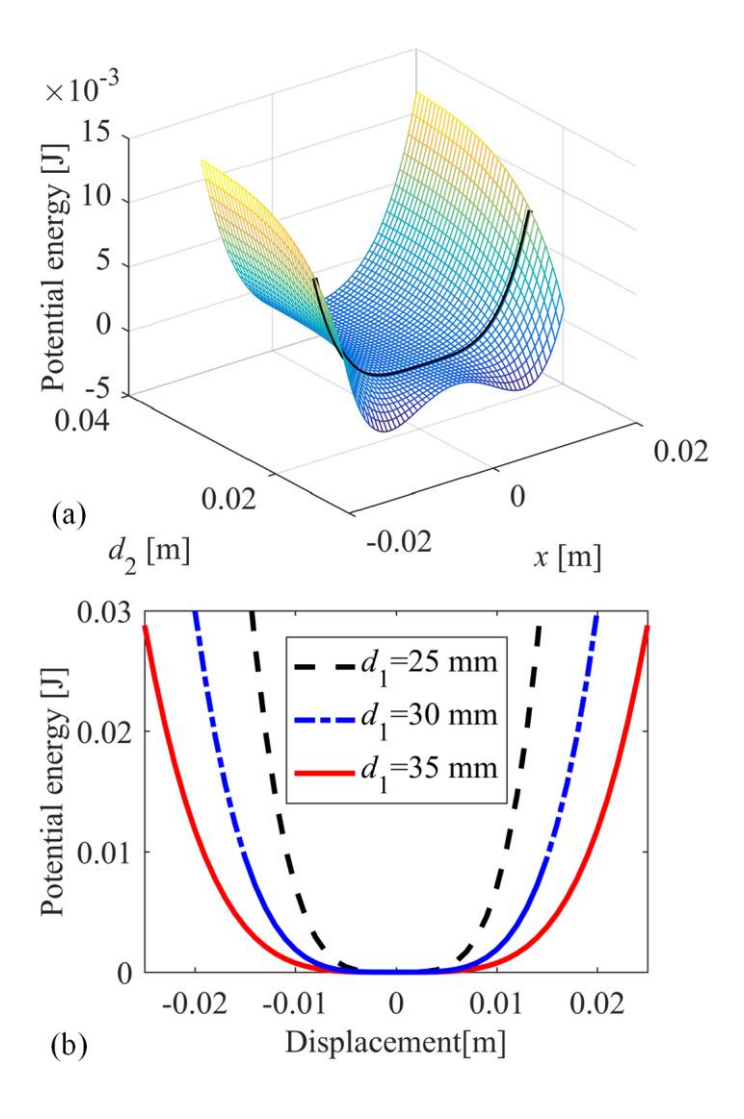


Fig. 3 (a) Potential energy functions for $d_1 = 30$ mm when with different values of d_2 ; (b) potential energy function for QZS-EMEHs with d_1 equaling 25 mm, 30 mm, and 35 mm.

As an example, Fig. 3 (a) illustrates the variation of the potential energy function with the value of d_2 when $d_1 = 30$ mm. When d_2 is small, the configuration exhibits the characteristic of a bistable system. With an increase in d_2 , the potential energy function gradually becomes flat and then appears to be a monostable configuration. When $d_2 = 19.55$ mm, the configuration has a very flat potential energy function, as shown by the blue line in Fig. 3 (b), and exhibits the characteristic of a quasi-zero

stiffness system. In addition, Fig. 3 (b) illustrates the potential energy functions of the QZS-EMEHs when $d_2 = 25$ mm and $d_2 = 35$ mm. It can be seen from Fig. 3(b) that the potential energy function has a wider zone, in which it is close to zero, with an increase in the value of the parameter d_1 .

For the configuration described above, we assume that the displacement of the rolling magnet D is represented by y_D , under a base displacement excitation with an expression of x_b . In this condition, the displacement of the rolling magnet D relative to the base can be expressed as $x=y_D-x_b$. Then, the kinetic energy and potential energy[33] of the rolling magnet D can be respectively expressed as

$$T = \frac{1}{2}m\left(x_{\mathcal{E}}^2 + x_{\mathcal{E}}^2\right)^2 + \frac{1}{2}I_{\mathcal{E}}\theta^{2} \tag{4}$$

$$U = \int F_{mt} dx \tag{5}$$

where m is the mass of the rolling magnet. In Eq. (4), I_c is the rotational inertia of the rolling magnet expressed as $\frac{1}{2}mr_1^2$ and θ^8 is the angular velocity of rotation calculated by $\frac{\mathcal{R}}{r_1}$. Based on the

Lagrange equation [34], the dynamic model of the QZS-EMEHs can be expressed as follows.

$$\frac{3}{2}m + c_d + F_{mt} = -m + c_d \tag{6}$$

where c_d is the damping which is expressed as the sum of the mechanical damping c_m and electric damping c_e . When a load resistance is connected with the coils[21], the electric damping c_e can be calculated as Eq. (7).

$$c_e = \frac{\alpha^2}{R_{\text{int}} + R_{load}} \tag{7}$$

Furthermore, the voltage across the load resistance can be expressed as

$$V_{load} = \frac{\alpha \dot{x}}{\left(R_{int} + R_{load}\right)} R_{load} \tag{8}$$

where R_{int} is the internal impedance of the coil, R_{load} is the external load resistance, and α is the electromechanical coupling coefficient. In this paper, the parameters applied in the following

theoretical and numerical investigations are set as m = 0.0059 kg, $c_{\rm m} = 0.01$ N/m, $R_{\rm int} = 190$ Ω , $R_{\rm load} = 1$ M Ω , $\alpha = 2.15$ N/A unless other values are assigned. Regarding the coefficients of the polynomial, they are shown in Table. 1 for different values of the parameter d_1 .

Table. 1 Coefficient of the fitted polynomial.

	$d_1 = 25 \text{ mm}$	$d_1 = 30 \text{ mm}$	$d_1 = 35 \text{ mm}$
$k_3 (\text{N/m}^3)$	2.8089×10^6	7.4986×10 ⁵	2.9332×10 ⁵
k_1 (N/m)	0.8898	0.1342	0.4432

3. Nonlinear dynamic analysis

3.1 Theoretical solution

To theoretically investigate the response of the QZS-EMEHs under harmonic excitation, the harmonic balance method is applied[35]. If the base harmonic excitation is expressed as $x_b = A\cos(\omega t)$, the dynamic model described by Eq. (6) can be rewritten as

$$\frac{3}{2} \approx 2\xi \omega_n + \omega_n^2 x + \beta x^3 = F \cos \omega t \tag{9}$$

where

$$\omega_n = \sqrt{k_1/m}, \ \xi = \frac{c_d}{2m\omega_n}, \ F = \omega^2 A, \ \beta = \frac{k_3}{m}$$
 (10)

According to the harmonic balance method, the displacement response in Eq. (9) can be assumed as

$$x = a\sin(\omega t) + b\cos(\omega t) \tag{11}$$

By substituting the assumed solution into Eq. (9), neglecting the time derivative terms and balancing the terms multiplied by $\sin(\omega t)$ and $\cos(\omega t)$, the following equations are obtained:

$$-\frac{3}{2}a\omega^{2} - 2\xi\omega_{n}\omega b + \omega_{n}^{2}a + \frac{3}{4}\beta a(a^{2} + b^{2}) = 0$$
 (12)

$$-\frac{3}{2}b\omega^{2} + 2\xi\omega_{n}\omega a + \omega_{n}^{2}b + \frac{3}{4}\beta b(a^{2} + b^{2}) = F$$
 (13)

The amplitude of the displacement response expressed as $r = \sqrt{a^2 + b^2}$ can be calculated as

$$\left[-\frac{3}{2}\omega^2 + \omega_n^2 + \frac{3}{4}\beta r^2 \right]^2 r^2 + \left(2\xi\omega_n\omega\right)^2 r^2 = F^2$$
 (14)

Regarding the voltage across the load resistance, its theoretical expression is as follows.

$$V_{load} = \frac{\alpha r \omega}{\left(R_{int} + R_{load}\right)} R_{load} \tag{15}$$

When the excitation level is 1 m/s², the numerical displacement and voltage response of the three QZS-EMEHs with $d_1 = 25$ mm, $d_1 = 30$ mm, and $d_1 = 35$ mm under up and down-sweep frequency excitations is illustrated in Fig. 4 (a), (b), and (c), along with the theoretical results calculated from Eq. (14) and (15). Under up-sweep frequency excitation, the displacement response of the QZS-EMEH with $d_1 = 25$ mm first increases with an increase in the excitation frequency and then jumps down at 15.1 Hz, with a maximum displacement of 6 mm obtained. For the down-sweep frequency excitation, the jump-up frequency is 4.8 Hz and the maximum displacement response is 2.8 mm. In the frequency range between the jump-up (4.8 Hz) and jump-down (15.1 Hz) frequencies, there exist multiple solutions respectively on the high and low-energy orbits. For the voltage response, it exhibits the same variation trend as the displacement response, and the maximum voltage under up and down-sweep frequency are respectively 1.0 V and 0.22 V.

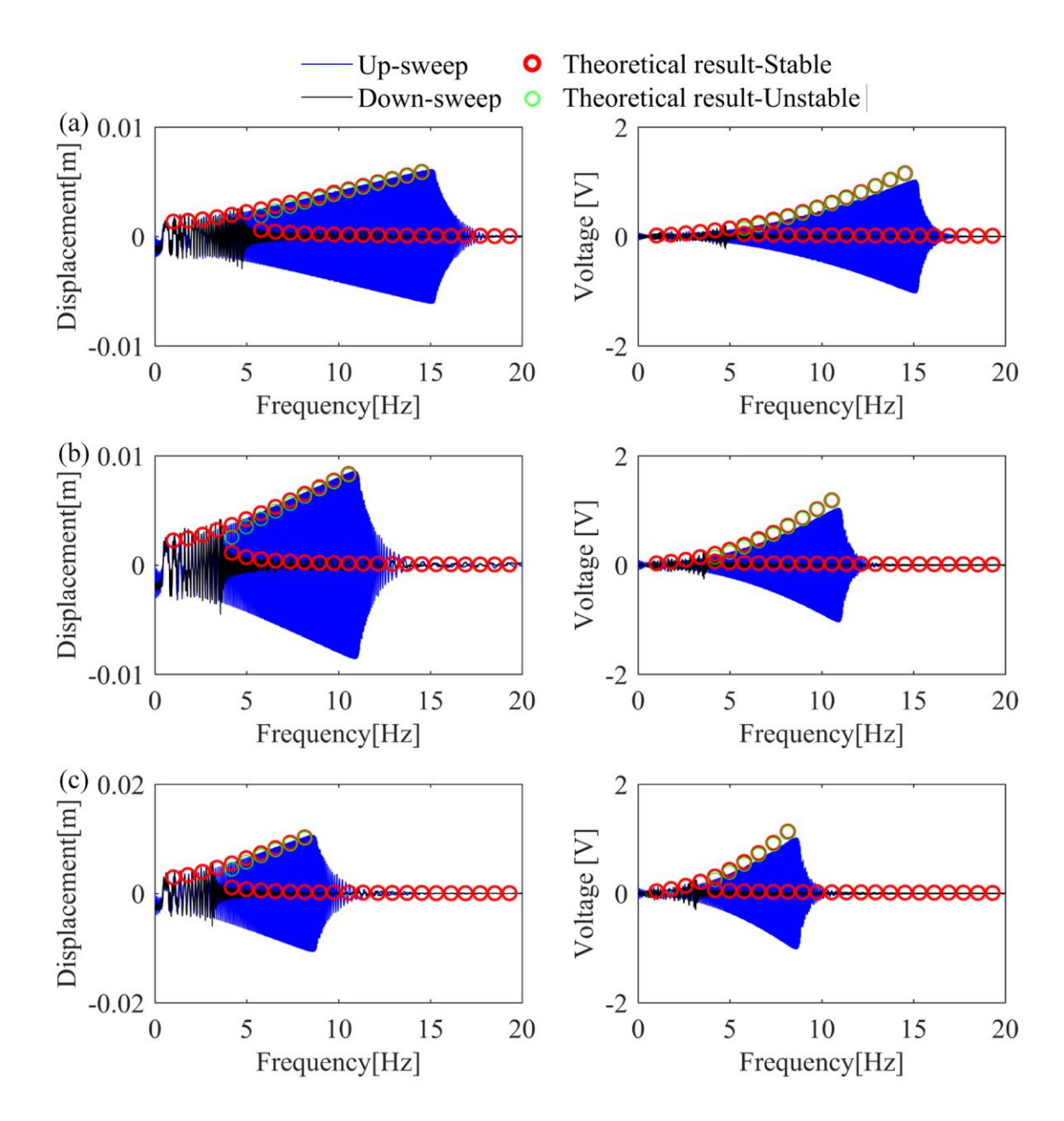


Fig. 4 Numerical and theoretical displacement and voltage response of the QZS-EMEHs under sweep frequency excitation with a excitation of 1 m/s²: (a) $d_1 = 25$ mm; (b) $d_1 = 30$ mm; (c) $d_1 = 35$ mm.

With an increase in the value of d_1 , the variation trend of the displacement and voltage is not influenced. For the case of $d_1 = 30$ mm, the maximum displacement and voltage under up-sweep frequency excitation are respectively 8.5 mm and 1.0 V at the jump-down frequency of 10.9 Hz, while they are 4.3 mm and 0.26 V at the frequency of 3.53 Hz under down-sweep frequency

excitation, as in Fig. 4 (b). With the increase of d_1 , it is observed that the jump frequency decreases, while the peak displacement exhibits an increase. The reason for this phenomenon is due to that the potential energy function has a wider zone in which it is close to zero for a larger value of d_1 , as illustrated in Fig. 3 (b). As d_1 increases to 35 mm, the jump frequencies in Fig. 4 (c) under up and down-sweep frequency excitations are 8.65 Hz and 3.1 Hz, and the peak displacements are respectively 10.7 mm and 5.7 mm, along with the peak voltages of 1.0 V and 0.3 V. It should be noted that the theoretical displacement responses are in good agreement with the numerical simulations, while the analytical voltage response exhibits a slightly larger value than the numerical simulation.

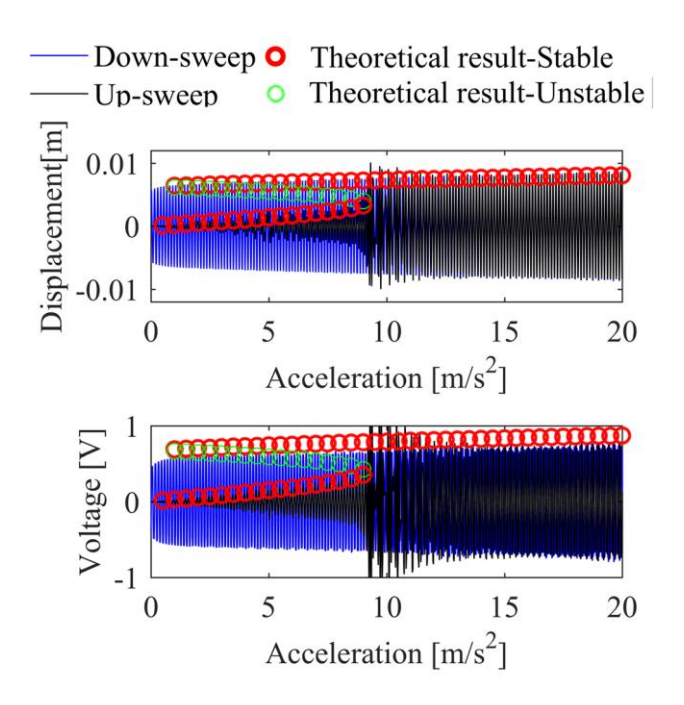


Fig. 5 Numerical and theoretical displacement and voltage response of the QZS-EMEH with $d_1 = 30$ mm under sweep acceleration excitation with a frequency of 8 Hz.

In addition to the response under sweep frequency excitation, the output under different acceleration levels is also investigated to compare with the analytical results. Fig. 5 shows the displacement and voltage response of the QZS-EMEH when $d_1 = 30$ mm under up and down-sweep

acceleration excitation for a frequency of 8 Hz from simulation and theoretical analysis. During up-sweep acceleration excitation, the displacement and voltage both increase with an increase in the excitation level and then jumps to a high-energy orbit at an acceleration of 9.45 m/s², showing a good agreement with the theoretical outcomes. However, for down-sweep acceleration excitation, the QZS-EMEH are always oscillating on the high-energy orbit.

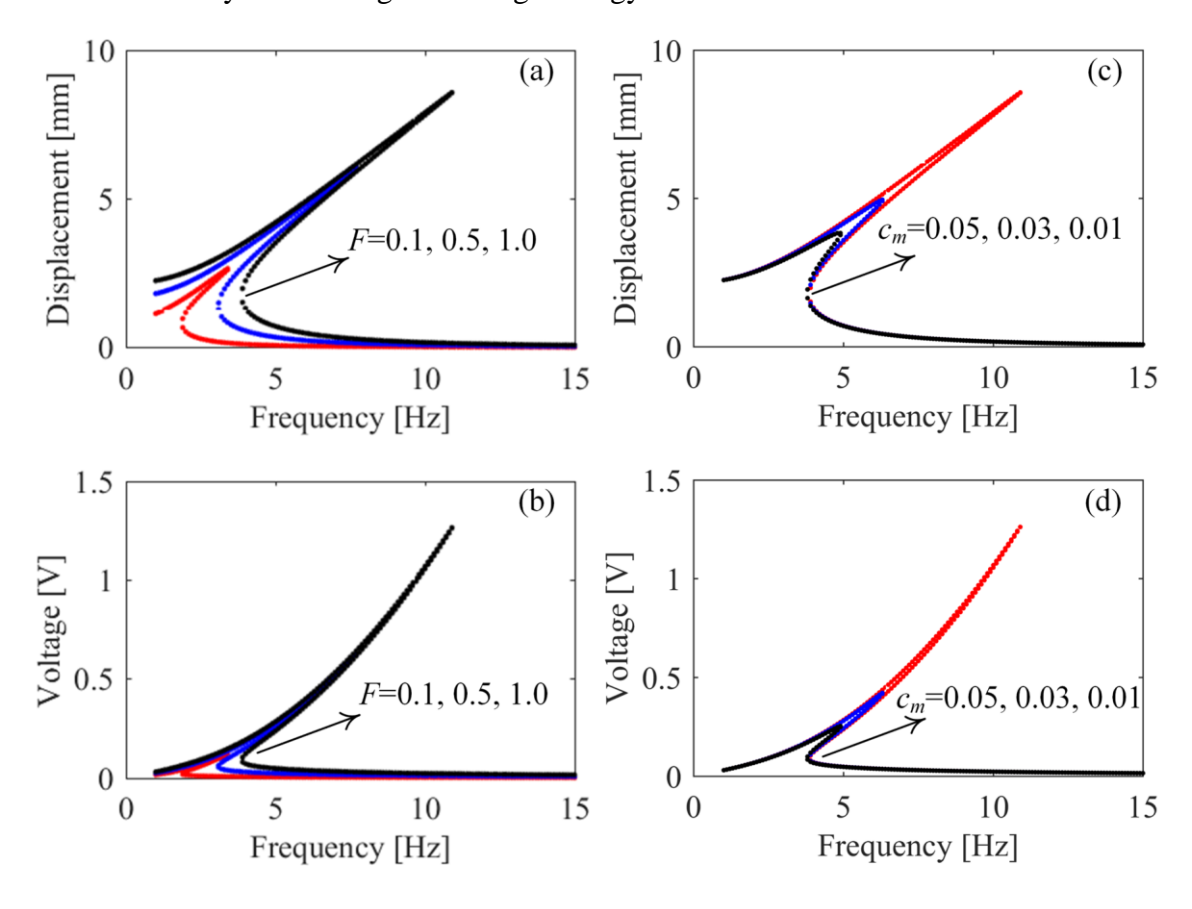


Fig. 6 Influence of excitation level and mechanical damping on displacement and voltage response.

Based on the theoretical solutions from the harmonic balance method, the influence of the system parameters on the energy harvesting performance of the QZS-EMEHs is now discussed. Fig. 6 (a) and (b) illustrate the influence of excitation level on the displacement and voltage response. It is seen that the increase in excitation level not only has a positive effect on the peak displacement and voltage but also increases the jump frequencies. For the excitation levels of 0.1 m/s², 0.5 m/s², and 1 m/s², the jump down frequencies are 3.4 Hz, 7.7 Hz, and 10.9 Hz, respectively, along with peak

voltages of 0.12 V, 0.63 V, and 1.26 V. Therefore, the output performance of the QZS-EMEH can be greatly enhanced by increasing the excitation level. Concerning the mechanical damping, Fig. 6 (c) and (d) show its influence on the displacement and voltage response under excitation with a level of 1 m/s². Clearly, with a decrease in the mechanical damping, the peak displacement and voltage of the QZS-EMEH increase significantly. In addition, the influence of external load resistance and electromechanical coupling coefficient on the response characteristics are also examined, and the results are shown in Fig. 7 (a) ~ (d). By decreasing the external load resistance, the electrical damping is increased as seen in Eq. (7), thus decreasing the peak displacement, voltage, and jump frequencies. Regarding the electromechanical coupling coefficient, its increase has almost no effect on the electrical damping for the QZS-EMEH with large internal resistance. Therefore, the displacement response is almost not affected, while in contrast, the output voltage is enhanced, according to Eq. (15), with an increase in electromechanical coupling coefficient.

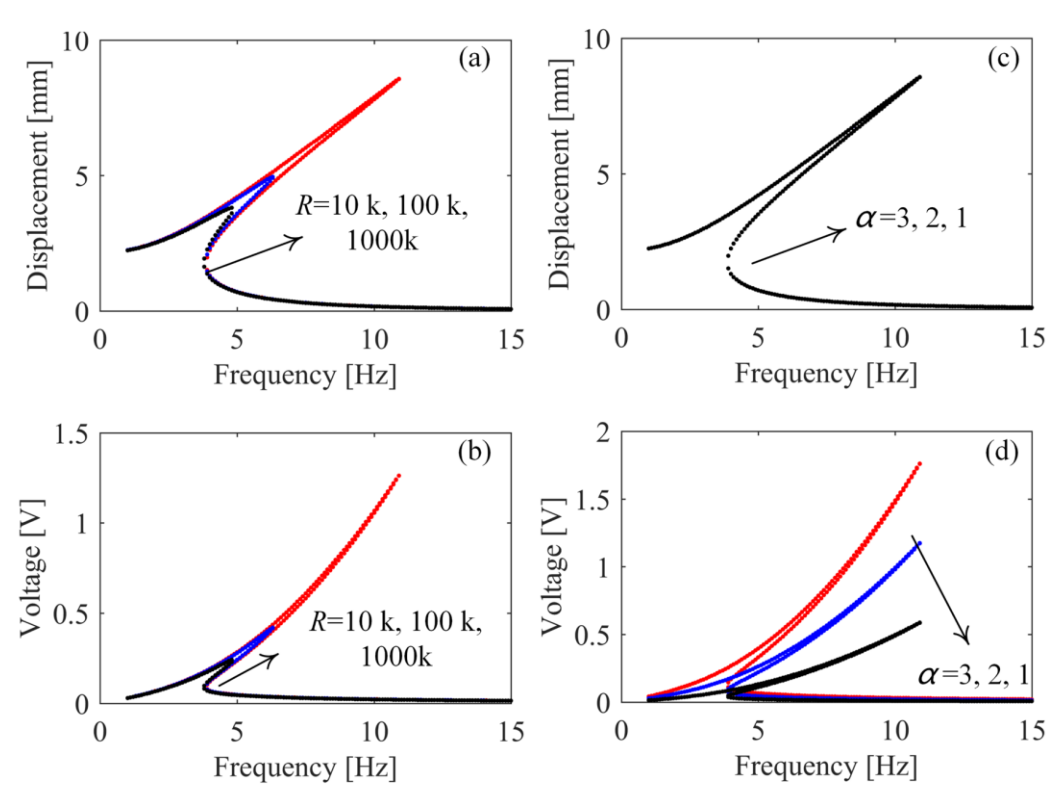


Fig. 7 Influence of external load resistance and electromechanical coupling coefficient on

displacement and voltage response.

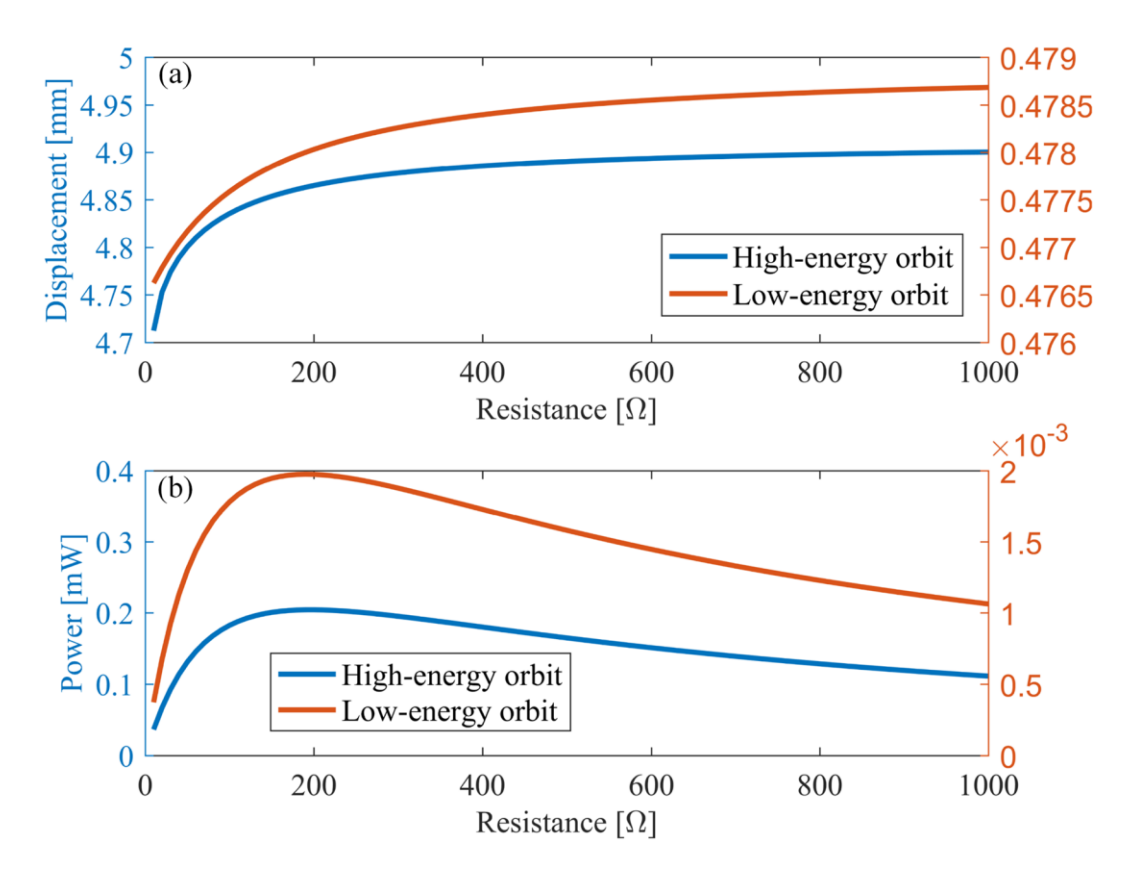


Fig. 8 Influence of load resistance on the displacement response and maximum output power under harmonic excitation of 1 m/s² and 6 Hz.

Under harmonic excitation with a level of 1 m/s² and a frequency of 6 Hz, the displacement response of the QZS-EMEH with $d_1 = 30$ mm for varying external load resistance is shown in Fig. 8 (a), where the blue line represents the oscillation on the high-energy orbit, while the red line is the low-energy orbit. It is seen that an increase in the external load resistance leads to an increase in the displacement, and this phenomenon is due to that the external load resistance has a negative influence on the electrical damping. Regarding the output power in Fig. 8 (b), it initially increases and then decreases with an increase in external load resistance, and achieves the maximum power when the external load resistance equals the internal resistance, namely $R_{\text{load}} = R_{\text{int}} = 190 \Omega$. To be noted, the maximum power obtained in the high-energy orbit is 0.2 mW, while it is about 0.002 mW

in the low-energy orbit. With the optimum resistance (190 Ω) connected, the output power of the three QZS-EMEHs with $d_1 = 25$ mm, $d_1 = 30$ mm, and $d_1 = 35$ mm under up and down-sweep frequency excitation with a level of 1 m/s² are shown in Fig. 9 (a), (b) and (c) respectively. The maximum output powers of the three QZS-EMEHs under up-sweep frequency excitation are all approximately 0.31 mW, while the jump down frequencies are respectively 10.35 Hz, 7.4 Hz, and 5.94 Hz for $d_1 = 25$ mm, 30 mm, and 35 mm. For down-sweep frequency excitation, the maximum output powers of the three QZS-EMEHs are 0.05 mW at 4.72 Hz, 0.07 mW at 3.53 Hz, and 0.09 mW at 3.1 Hz respectively.

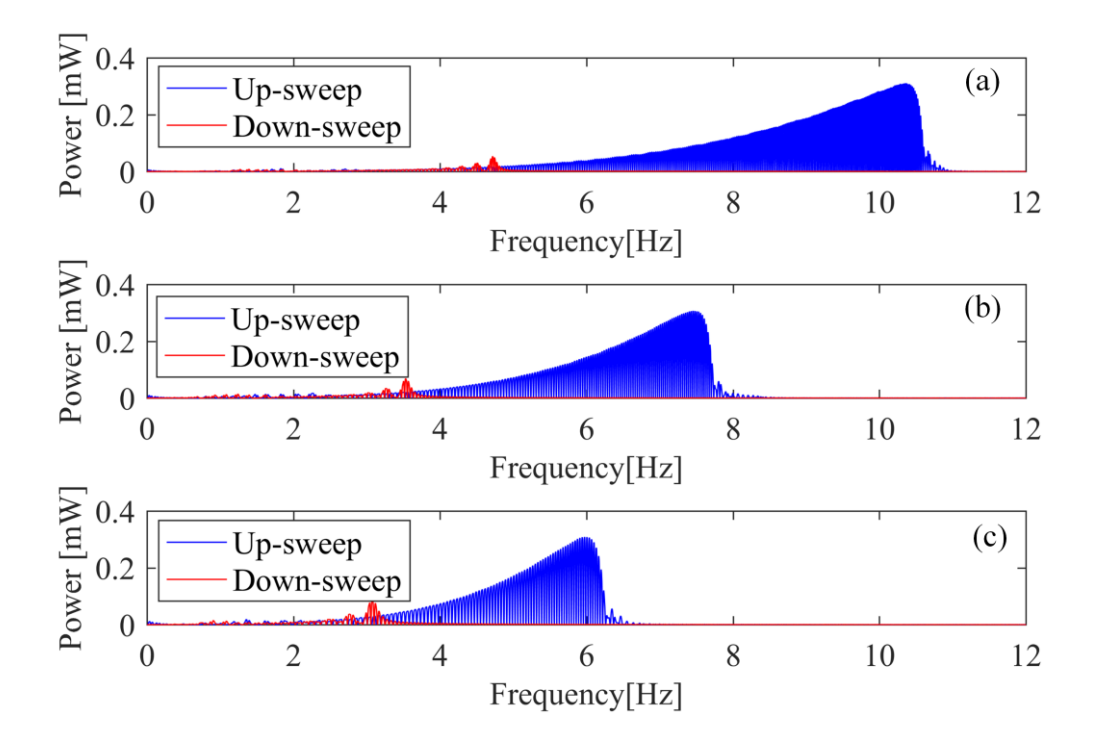


Fig. 9 Numerical output power of the QZS-EMEHs under sweep frequency excitation with an excitation of 1 m/s²: (a) $d_1 = 25$ mm; (b) $d_1 = 30$ mm; (c) $d_1 = 35$ mm.

3.2 Multiple solutions identification

As illustrated in Section 3.1, multiple solutions exist for the QZS-EMEHs under certain excitation conditions. However, the theoretical results from harmonic balance only consider the

periodic-1 vibration, which has the same frequency as the excitation. For the QZS-EMEHs, it may exhibit more complex nonlinear dynamic characteristics, such as subharmonic and superharmonic oscillation. As a result, we focus on the nonlinear dynamics of the QZS-EMEHs, in this section, in particular the multiple solutions characteristics.

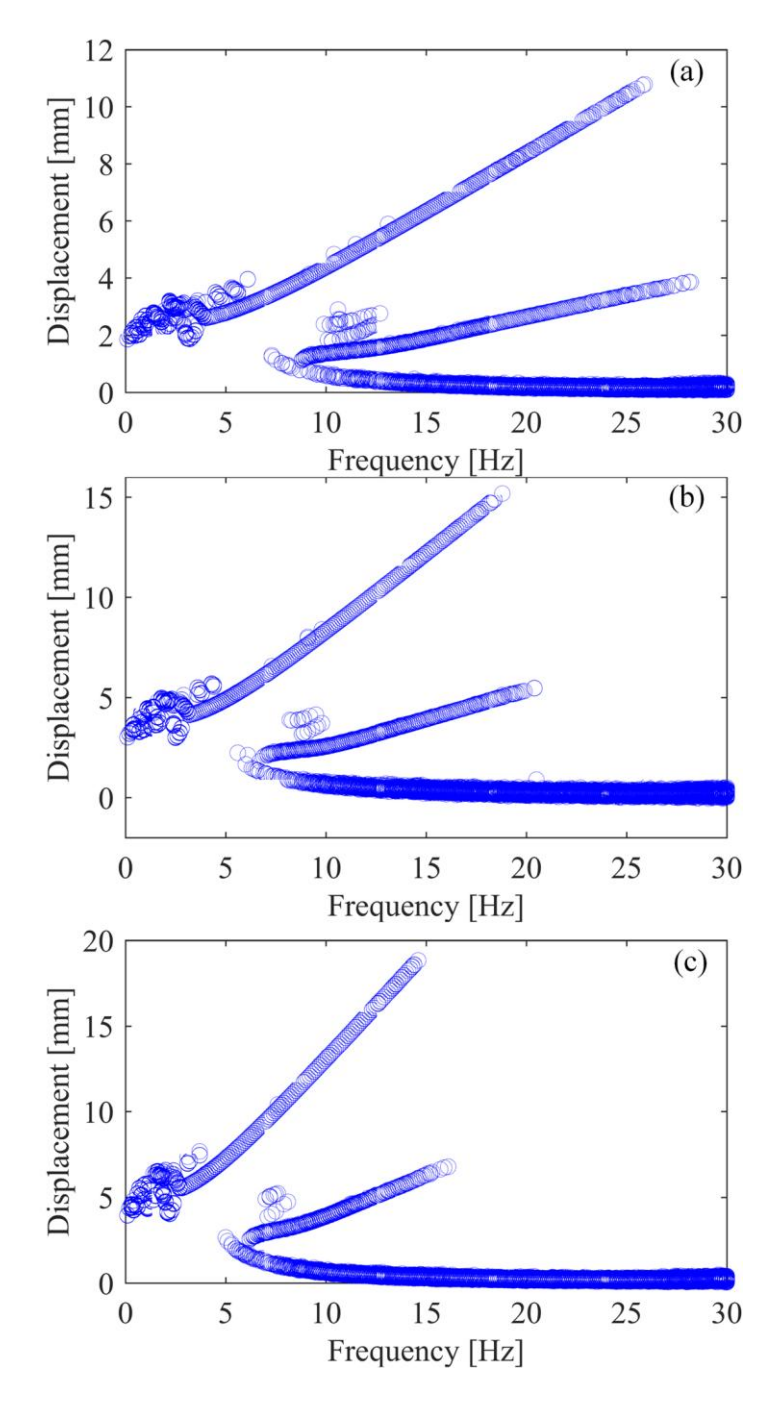


Fig. 10 Bifurcation diagram of peak displacement to frequency under an excitation of 3 m/s²: (a) d_1 = 25 mm; (b) d_1 = 30 mm; (c) d_1 = 35 mm. Note that, the simulation at each frequency is carried out 30

times with the initial position fixed at the static equilibrium position ($x_0 = 0$) while the initial velocity is a random number selected from -1.5 m/s to 1.5 m/s.

In Fig. 10 (a), (b), and (c), the bifurcation diagrams of the peak displacement to excitation frequency at an excitation of 3 m/s² are illustrated for the QZS-EMEHs with $d_1 = 25$ mm, $d_1 = 30$ mm, and $d_1 = 35$ mm. It should be noted that the numerical simulations are carried out 30 times at each frequency with the initial position at the static equilibrium position ($x_0 = 0$) while the initial velocity is a random number selected from -1.5 m/s to 1.5 m/s. From the diagram, three main branches are observed, along with several scattered points. These branches make it possible to approximately distinguish the oscillations on different orbits.

For the QZS-EMEH with $d_1 = 30$ mm, it is seen from Fig. 10 (b) that the system can achieve a relatively large displacement, even at very low frequencies. With an increase in the excitation frequency, the peak displacement response on the high-energy orbit exhibits an increasing trend, and the high-energy orbit oscillation continues until a frequency of 19.2 Hz. Starting from 5.6 Hz, the QZS-EMEH begins to oscillate in the low-energy and middle-energy orbits. The peak displacement decreases with an increase in the excitation frequency when the oscillation is in the low-energy orbit, while it exhibits the peak displacement increasing with frequency in the middle-energy orbit. In particular, the cut-off frequency for the middle-energy orbit oscillation is approximately 20.4 Hz. Another point to note is that some scattered points are distributed around a frequency of 9 Hz, indicating more complex dynamic behavior.

To further understand the nonlinear dynamic behavior, the response characteristics of the QZS-EMEH with $d_1 = 30$ mm under several specific excitation frequencies are examined in more detail. When the excitation frequency is 2.5 Hz, the displacement, voltage, phase orbit, Poincaré map,

and frequency spectrum of the voltage, of two possible solutions of the QZS-EMEH are shown in Fig. 11 (a) and (b). From the displacement response and phase orbit, the two possible solutions exhibiting different peak displacements can be identified. However, the different displacement responses do not influence the output voltage and a peak voltage of 0.22 V is achieved. In the frequency spectrum of the voltage, the energy not only distributes at the main frequency of 2.5 Hz, which equals the excitation frequency, but also can be observed at the multiple of the excitation frequency, such as 5.0 Hz, 7.5 Hz, 10.0 Hz, and 12.5 Hz.

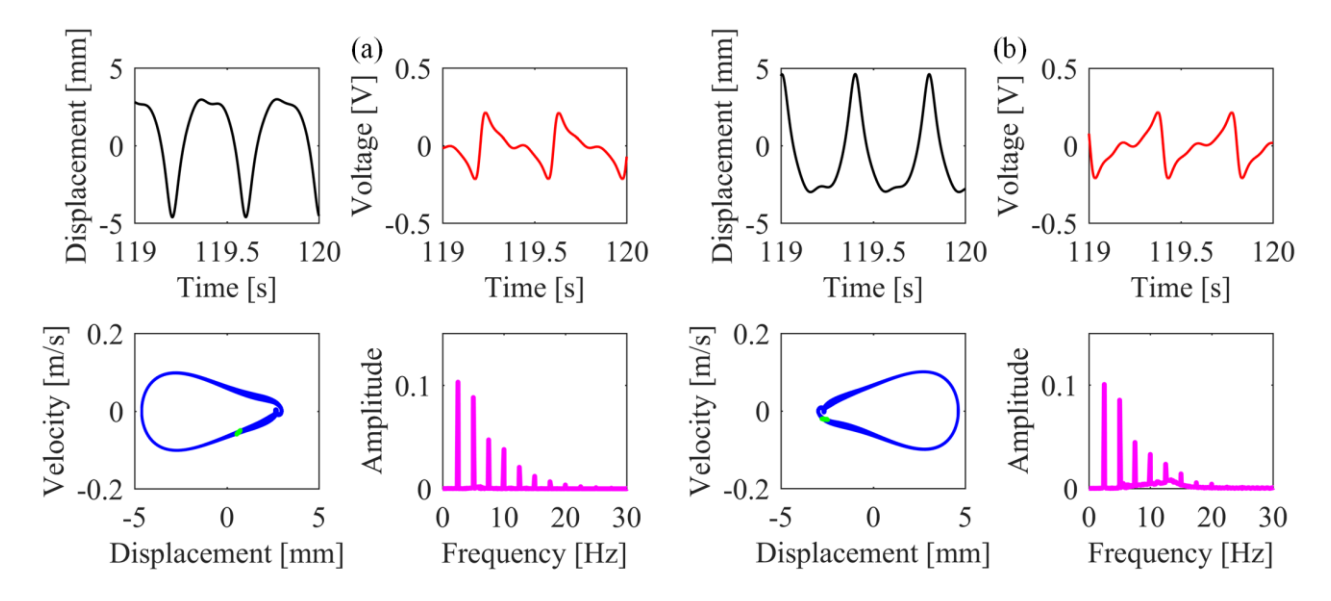


Fig. 11 Displacement, voltage, phase orbit, Poincaré map, and frequency spectrum of the QZS-EMEH with $d_1 = 30$ mm at an excitation of 3 m/s² and 2.5 Hz.

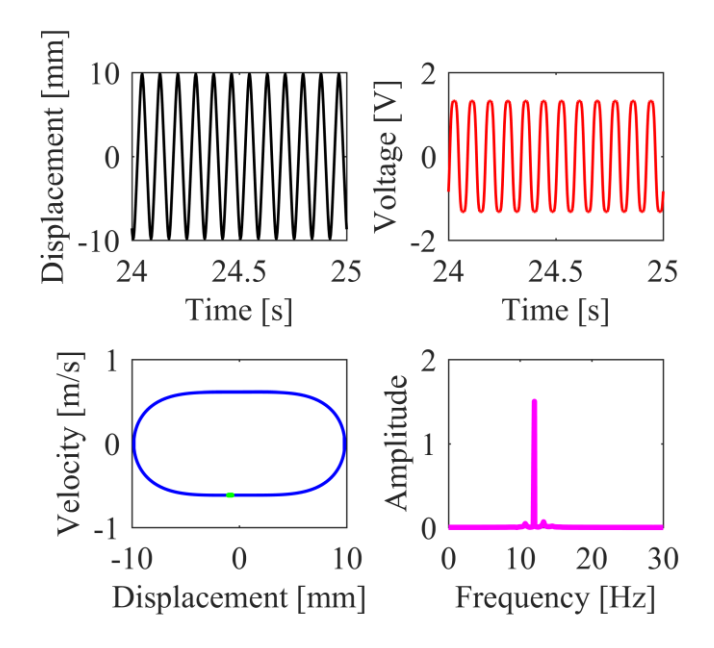


Fig. 12 Displacement, voltage, phase orbit, Poincaré map, and frequency spectrum of the QZS-EMEH with $d_1 = 30$ mm on the high-energy orbit at an excitation of 3 m/s² and 12 Hz.

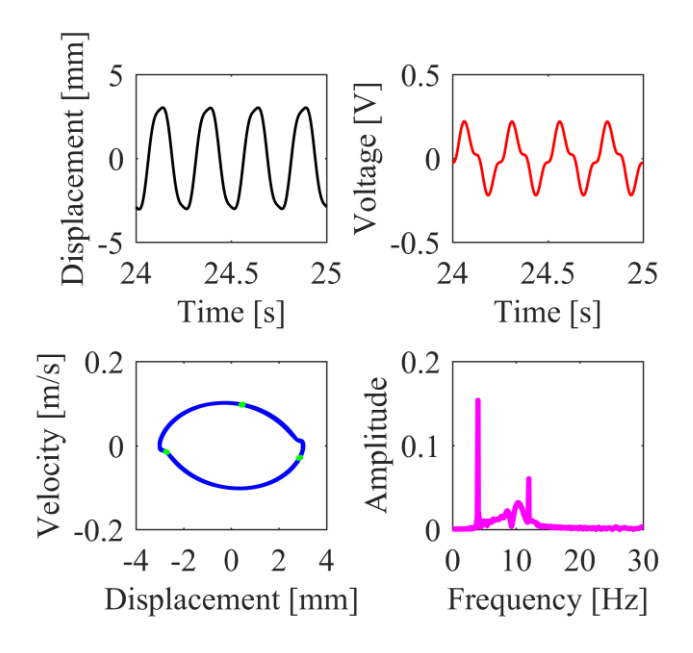


Fig. 13 Displacement, voltage, phase orbit, Poincaré map, and frequency spectrum of the QZS-EMEH with $d_1 = 30$ mm on the middle-energy orbit at an excitation of 3 m/s² and 12 Hz.

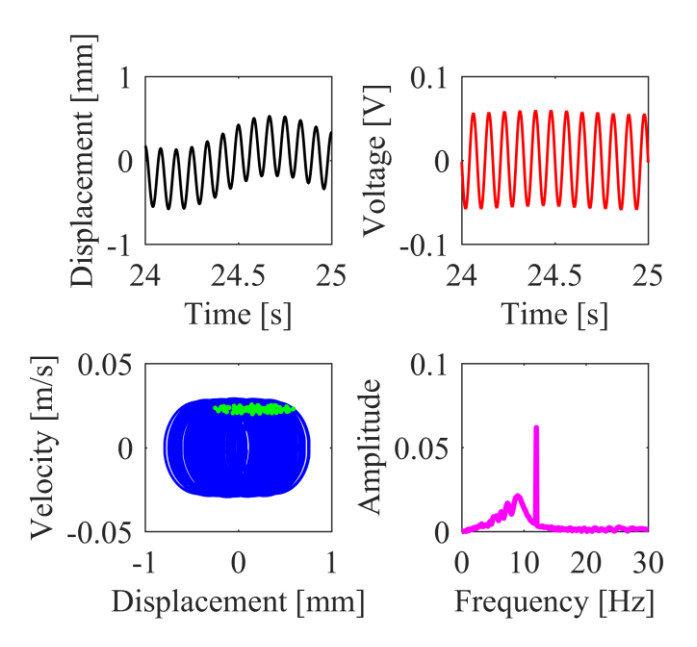


Fig. 14 Displacement, voltage, phase orbit, Poincaré map, and frequency spectrum of the QZS-EMEH with $d_1 = 30$ mm on the low-energy orbit at an excitation of 3 m/s² and 12 Hz.

As the excitation frequency increases to 12 Hz, the displacement, voltage, phase orbit, Poincaré map, and frequency spectrum of the voltage, of the QZS-EMEH on the high-energy orbit are shown in Fig. 12. The phase orbit identifies the high-energy orbit oscillation of the QZS-EMEH, and the isolated point in the Poincaré map and the single spectrum line in the frequency spectrum indicates a single-period oscillation. On this occasion, the obtained peak displacement and voltage responses are 9.83 mm and 1.32 V, respectively. When the initial velocity changes, a different oscillation type is obtained on the middle-energy orbit, and the displacement, voltage, phase orbit, Poincaré map, and frequency spectrum of the voltage are shown in Fig. 13. A peak voltage of 0.22 V is obtained along with a maximum displacement of 3 mm. From the frequency spectrum, it is seen that the main frequency component of the voltage is at 4 Hz, indicating that it is a 1/3 order subharmonic response originating from the nonlinearity. Furthermore, three isolated points are observed in the Poincaré map. In addition, different initial velocities lead to the oscillation of the QZS-EMEH on the low-energy orbit, and the corresponding numerical results are shown in Fig. 14. The single periodic

oscillation on the low-energy orbit results in a response frequency equaling the excitation frequency and the obtained peak voltage is only 0.06 V. In addition to the oscillations on the three main orbits, the scattered points in Fig. 10 (b) that are distributed around 9 Hz between high and middle-energy orbits are also clarified and the results indicate that they represent two oscillation types, similar to that shown in Fig. 11 (a) and (b).

For the QZS-EMEHs with $d_1 = 25$ mm and $d_1 = 35$ mm, the bifurcation diagrams of the peak displacement to excitation frequency under excitation of 3 m/s² are shown in Fig. 10 (a) and (c) respectively, and they exhibit the same characteristics as the QZS-EMEH with $d_1 = 30$ mm. For a QZS-EMEH with $d_1 = 25$ mm, the cut-off frequencies for the oscillation on high and middle-energy orbits are 25.9 Hz and 28.2 Hz respectively, while the starting frequency for low-energy orbit oscillation is approximately 7.3 Hz. As d_1 increases to 35 mm, the numerical results shown in Fig. 10 (c) indicate that the three critical frequencies are 14.6 Hz, 16.1 Hz, and 5.0 Hz respectively. By comparing the results in Fig. 10 (a), (b), and (c), it can be seen that an increase of d_1 decreases the cut-off frequencies for the oscillation on high and middle-energy orbits, and also decreases the starting frequency for low-energy orbit oscillation. This phenomenon may be due to that the potential energy function has a wider zone in which it is close to zero for a larger value of d_1 .

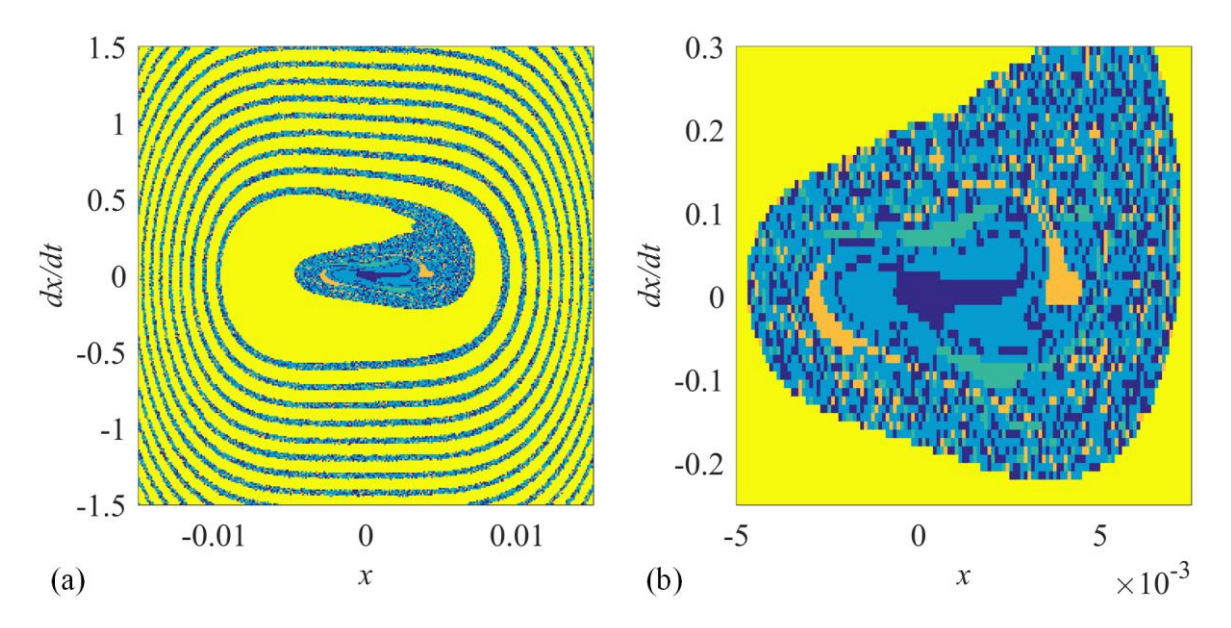


Fig. 15 Basin of attraction for the QZS-EMEH with $d_1 = 30$ mm under excitation of 3 m/s² and 8.9 Hz.

To investigate the influence of initial conditions on the response, basins of attraction are applied to illustrate the multiple solutions characteristics and sensitivity of the QZS-EMEHs. For the QZS-EMEH with $d_1 = 30$ mm, Fig. 15 (a) illustrates the basin of attraction when the excitation is with a level of 3 m/s² and a frequency of 8.9 Hz. In particular, the enlarged view in the range of [-0.005, 0.007, -0.3, 0.3] is emphasized in Fig. 15 (b). In the figure, the yellow area occupying 66.49% represents the oscillation with a final state in the high-energy orbits. This indicated that the QZS-EMEH has a larger probability to achieve large-amplitude motion to generate considerable outpower under excitation of 3 m/s² and 8.9 Hz. Regarding the oscillation on the middle and low-energy orbits, the light blue area and the dark blue area respectively indicate that the QZS-EMEH has the probability of 18.28 % and 8.98% to achieve the final states. In addition to the oscillations on the three main orbits, the QZS-EMEH has the same probability of 3.12% to achieve the two final states (green and orange area) illustrated in Fig. 11 (a) and (b), which are represented by scattered points in Fig. 10 (b).

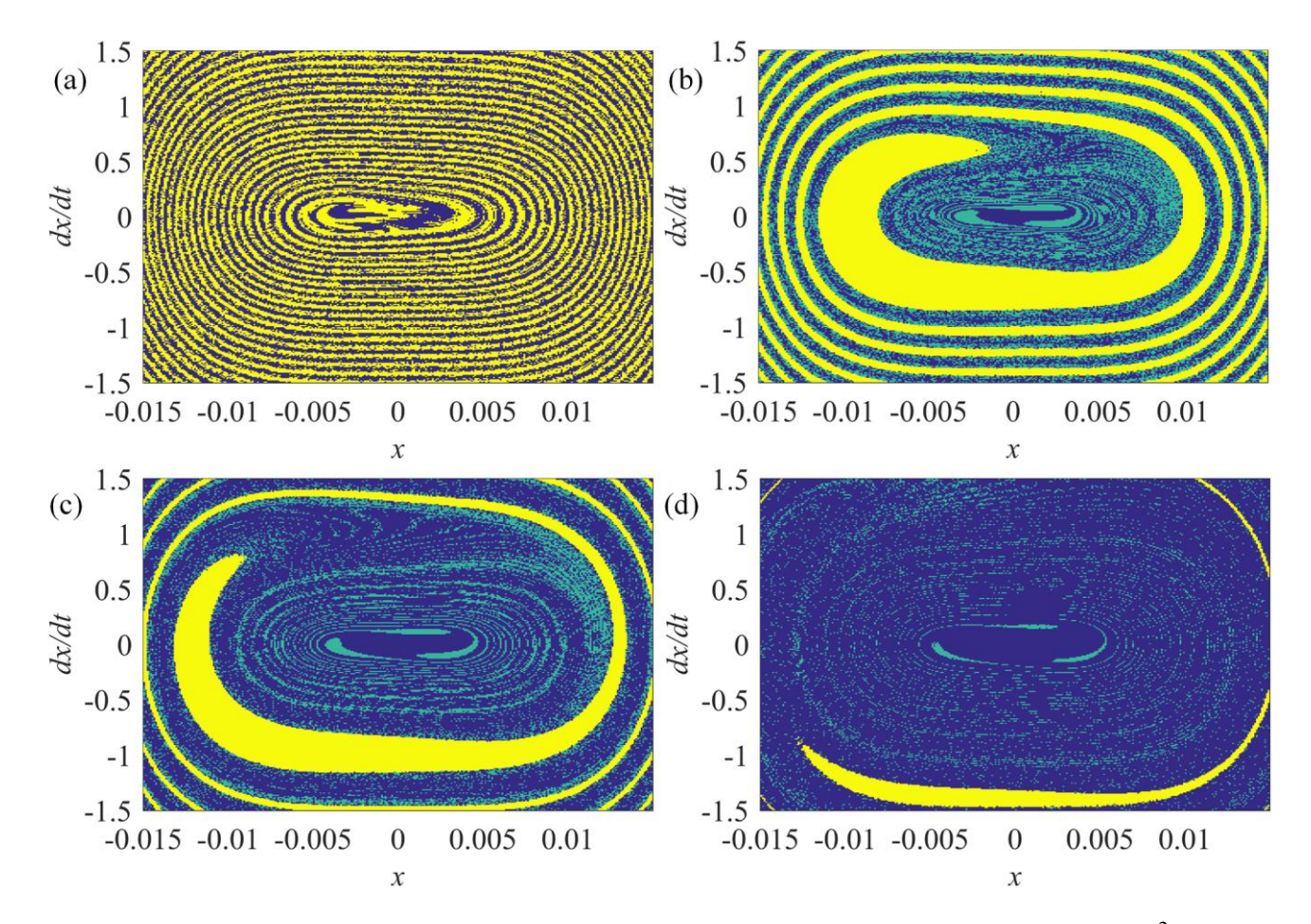


Fig. 16 Basins of attraction for the QZS-EMEH with $d_1 = 30$ mm under excitation of 3 m/s²: (a) 2.5 Hz; (b) 12 Hz; (c) 15 Hz; (d) 18 Hz.

In addition, Fig. 16 (a) describes the basin of attraction of the QZS-EMEH with $d_1 = 30$ mm under excitation of 3 m/s² and 2.5 Hz. On this occasion, only two final states illustrated in Fig. 11 (a) and (b) are obtained and the basin of attraction shows the probabilities are all 50%. As the frequency increases to 12 Hz, three final states shown in Fig. 12~14 are achieved and they are respectively represented by yellow, green, and dark blue areas, as shown in Fig. 16 (b), with the probabilities of 39.22%, 28.32%, and 32.46%. When the frequency is increased to 15 Hz, the probability to oscillate on the high and middle-energy orbits decreases to 19.31% and 19.9%, while a probability of 60.79% is obtained for achieving low-energy orbit vibration, as shown in Fig. 16 (c). As the frequency continues to increase to 18 Hz, the basin of attraction shown in Fig. 16 (d) illustrates the probabilities

to oscillate in the high and middle-energy orbits are only 4.35% and 8.5%, while the final state on the low-energy orbit is represented by a larger probability of 87.15%. Furthermore, the influence of excitation level on the sensitivity of the QZS-EMEHs is considered and the basins of attraction under excitation of 12 Hz are depicted in Fig. 17 (a) and (b) for the excitation levels of 2 m/s² and 4 m/s². It is observed that the excitation level has a significant influence on the final oscillation states of the QZS-EMEH. When the excitation level is 2 m/s², the probabilities to achieve high and middle-energy orbits are decreased to 23.50% and 20.47%, while larger probabilities of 49.31% and 28.52% are obtained for the larger excitation level of 4 m/s². Therefore, increasing the excitation level significantly increases the probability of the QZS-EMEH achieving large-amplitude oscillation to generate large output power.

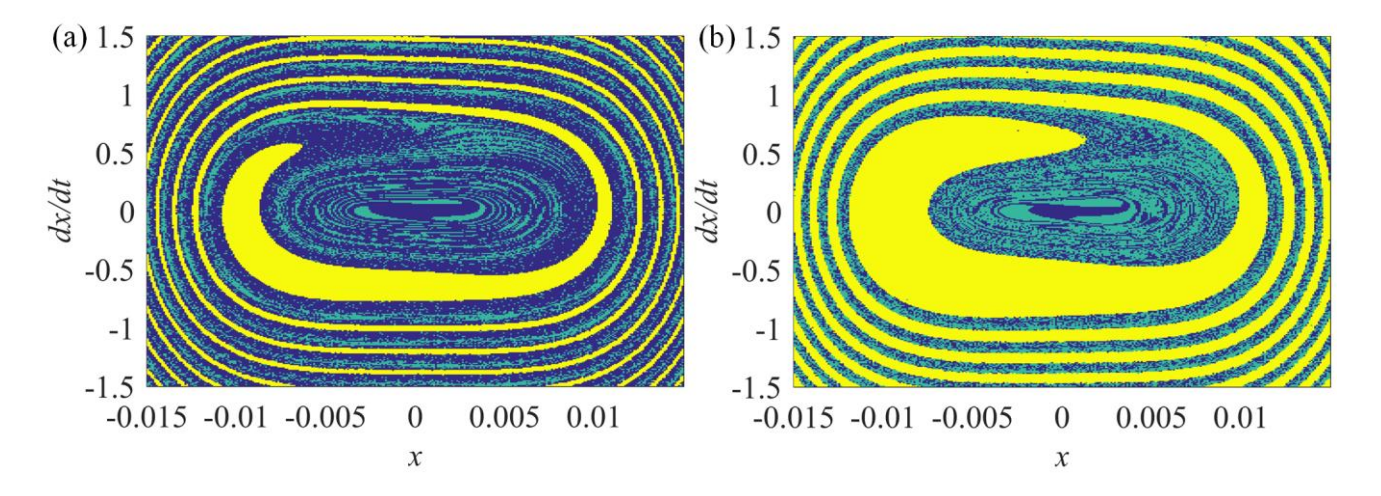


Fig. 17 Basins of attraction for the QZS-EMEH with $d_1 = 30$ mm under an excitation at a frequency of 12 Hz: (a) 2 m/s²; (b) 4 m/s².

4. Response under realistic ambient vibrations

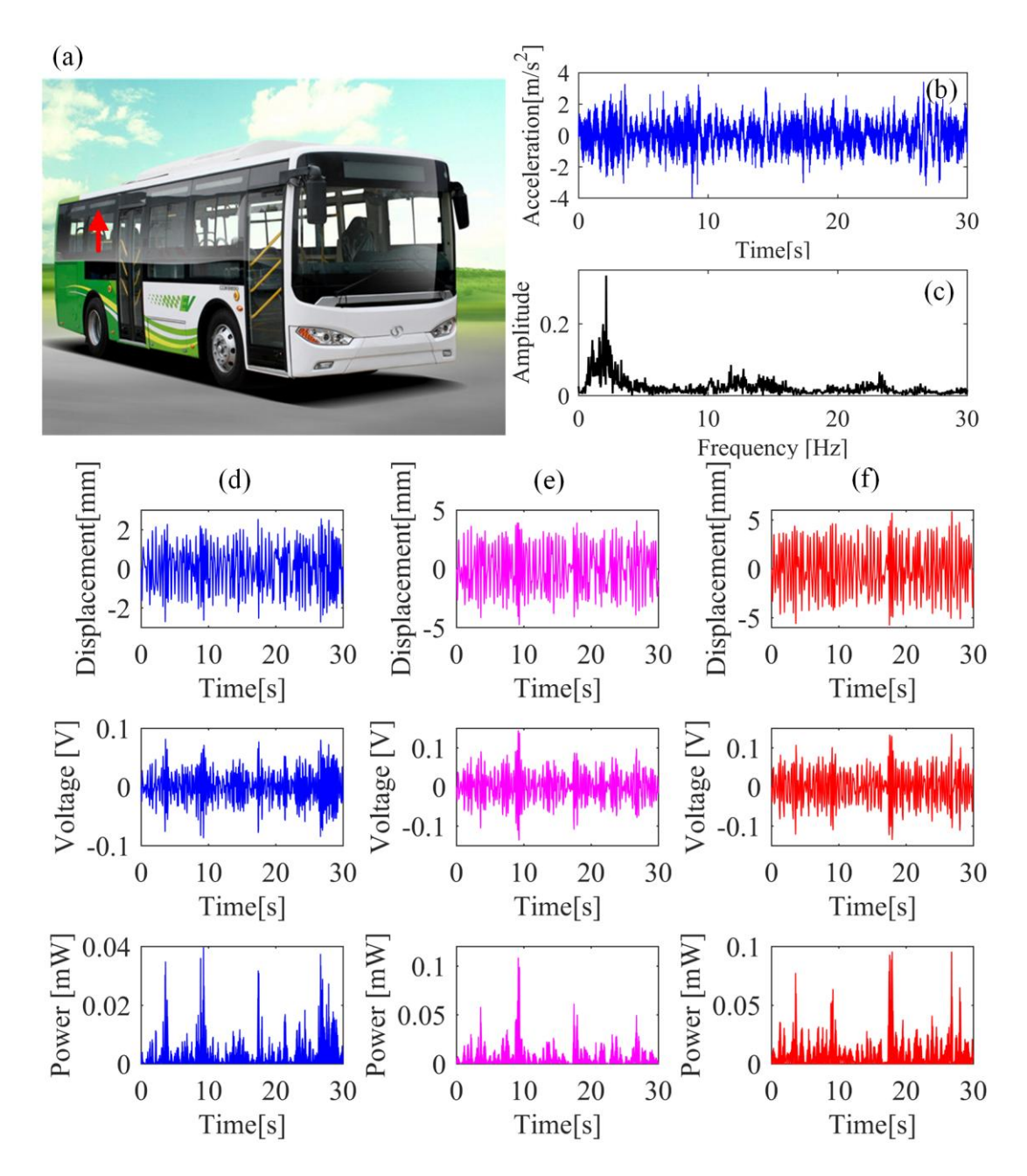


Fig. 18 Energy harvesting from the window of a bus: (a) position of acceleration measurement; (b) measured acceleration under driving conditions; (c) frequency spectrum. Displacement, voltage, and power response of the QZS-EMEHs: (d) $d_1 = 25$ mm; (e) $d_1 = 30$ mm; (f) $d_1 = 35$ mm.

In this section, we examine the energy harvesting performance of the QZS-EMEHs under realistic ambient vibrations, such as a bus and the human body. During the acceleration measurement of the bus, an acceleration sensor is attached at the lower edge of the window, as shown in Fig. 18 (a). When the bus rides smoothly, the obtained acceleration and corresponding frequency spectrum are

illustrated in Fig. 18 (b) and (c) respectively. It is seen that the acceleration fluctuates within a certain range with a peak value of approximately 4 m/s². From the frequency spectrum, it is identified that the main vibration frequencies are concentrated below 5 Hz, while there is little energy distributed at other frequencies. When the acceleration is applied to excite the QZS-EMEH with $d_1 = 25$ mm, the displacement, voltage, and output power response are shown in Fig. 18 (d). The QZS-EMEH can oscillate in a certain range of displacement and the peak displacement is 2.73 mm. Regarding the energy harvesting performance, the obtained maximum voltage is about 0.9 V, along with a peak power of 0.04 mW and average power of 0.003 mW. As d_1 increases to 30 mm, the QZS-EMEH oscillates in a larger displacement range with a peak displacement of 4.8 mm due to the variation in the potential energy function. On this occasion, the generated maximum voltage and output power are respectively 0.143 V and 0.12 mW, while the average power is 0.0065 mW. When the QZS-EMEH has $d_1 = 35$ mm, although the peak voltage is not enhanced, the average output power increases to 0.0093 mW.

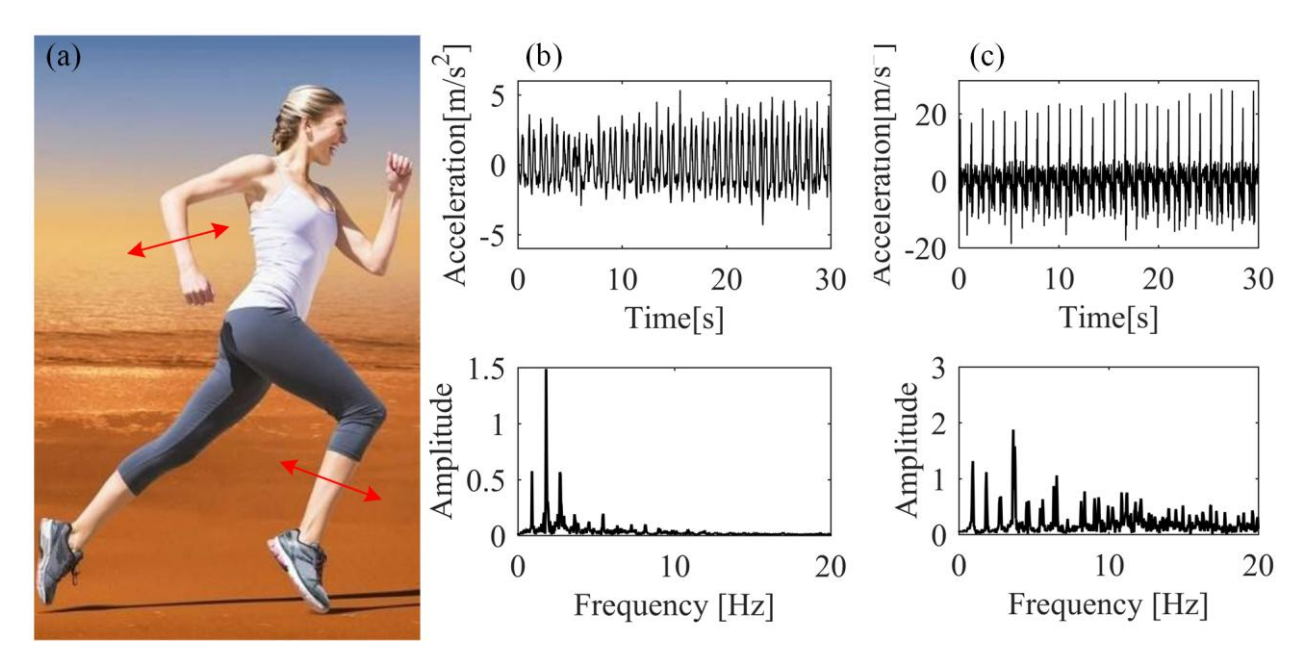


Fig. 19 (a) Direction of acceleration measurement; (b) measured acceleration from forearm and frequency spectrum; (c) measured acceleration from shank and frequency spectrum.

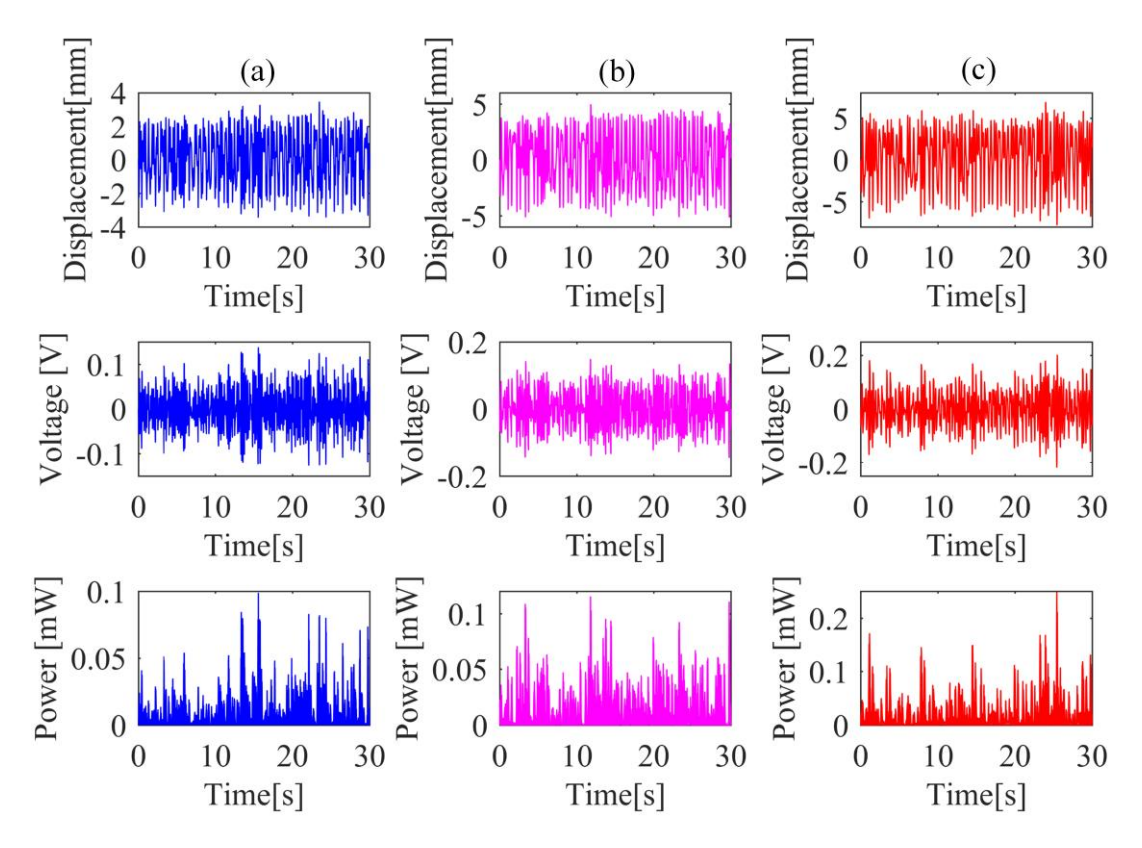


Fig. 20 Displacement, voltage, and power response of the QZS-EMEHs excited by acceleration from forearm: (a) $d_1 = 25$ mm; (b) $d_1 = 30$ mm; (c) $d_1 = 35$ mm.

In addition, the energy harvesting performance of the QZS-EMEHs under realistic human motion excitations is investigated. For the vibration signals of the human body, they are measured from the swing motion of the forearm and shank at a walking state, as shown in Fig. 19 (a). Fig. 19 (b) illustrates the measured acceleration from the forearm and the corresponding frequency spectrum. The peak acceleration is approximately 5.34 m/s² and it is observed from the frequency spectrum that the energy is distributed not only at the fundamental frequency (0.93 Hz) of human motion but also at 1.8 Hz and 2.7 Hz. When the acceleration is measured from the shank, the maximum acceleration obtained in Fig. 19 (c) is approximately 27 m/s², which is larger than that from the forearm because of the impact between the human leg and the ground.

When the acceleration from the forearm is applied as the input signals, the displacement, voltage, and power response of the QZS-EMEHs with $d_1 = 25$ mm, 30 mm, and 35 mm are shown in Fig. 20

(a), (b), and (c) respectively. The peak displacements of 3.45 mm, 5.1 mm, and 7.8 mm are respectively obtained for the three QZS-EMEHs, along with the maximum output voltages of 0.14 V, 0.15 V, and 0.22 V. Concerning the average output power, they are respectively 0.0093 mW, 0.0153 mW, and 0.0224 mW for the QZS-EMEHs with $d_1 = 25$ mm, 30 mm, and 35 mm. When the larger acceleration measured from the shank is applied to excite the QZS-EMEHs, the displacement, voltage, and power response shown in Fig. 21 indicate that the QZS-EMEHs could oscillate with larger displacement and generate a larger output voltage. The average output powers of the QZS-EMEHs with $d_1 = 25$ mm, 30 mm, and 35 mm are respectively 0.25 mW, 0.48 mW, and 0.26 mW.

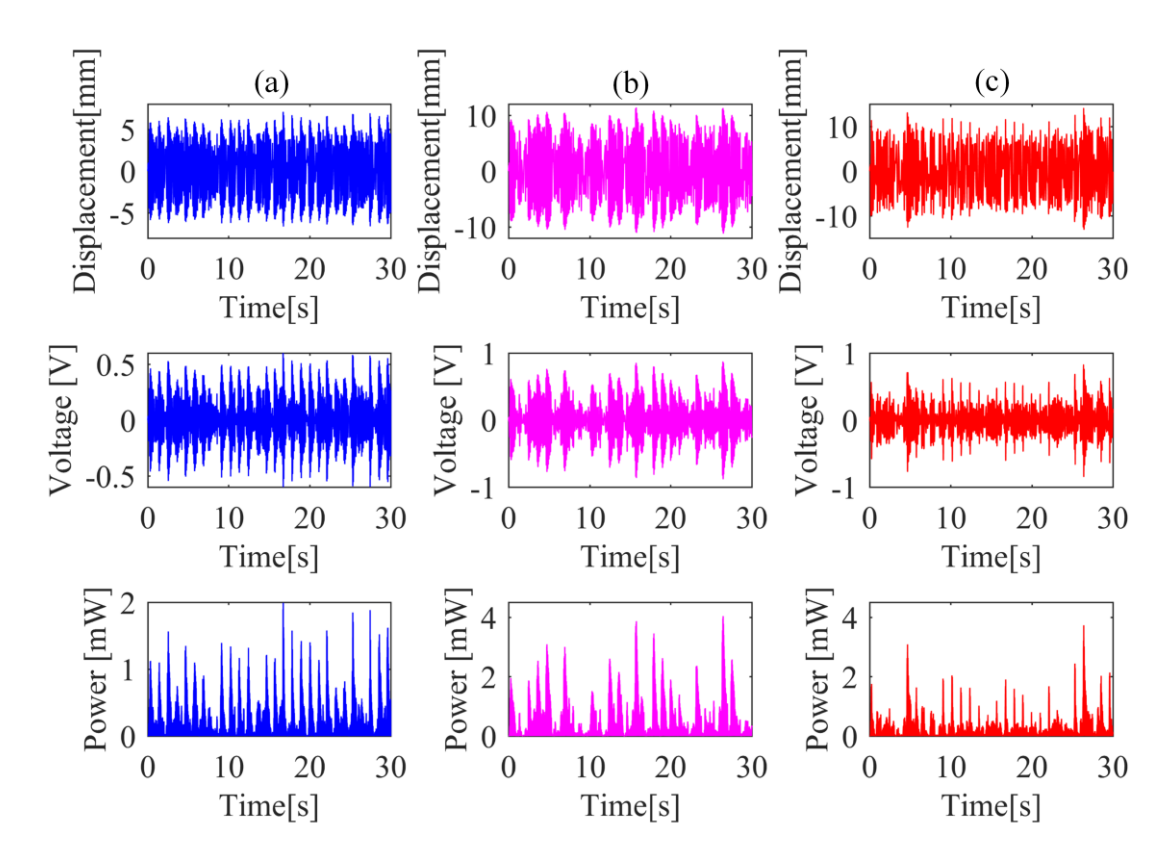


Fig. 21 Displacement, voltage, and power response of the QZS-EMEHs excited by acceleration from shank: (a) $d_1 = 25$ mm; (b) $d_1 = 30$ mm; (c) $d_1 = 35$ mm.

5. Conclusion

In this paper, a quasi-zero stiffness electromagnetic energy harvester (QZS-EMEH) utilizing a rolling magnet system is reported for energy harvesting from ultra-low frequency vibrations at low excitation levels. The QZS-EMEH is designed to exhibit small mechanical damping due to the rolling motion of a magnetically levitated magnet. Nonlinear restoring force exerted on the moving magnet is calculated according to Ansys Maxwell software and geometrical parameter relation, and the parameter region to achieve quasi-zero stiffness characteristics is emphasized. A dynamic model of the QZS-EMEH is established to predict the output and the theoretical solution is derived based on the method of harmonic balance. Numerical simulations under different excitation conditions verify the effectiveness of the theoretical solution and the influence of system parameters on the output performance of the QZS-EMEHs is investigated analytically. Our results indicate that an increase in excitation level and electromechanical coupling coefficient has a positive influence on the output, while the increase in mechanical damping degrades the performance. Concerning the external load resistance, an increase can broaden the response band, while there exists an optimum value to maximize the power for a given excitation frequency.

To understand the characteristics of multiple solutions, bifurcation diagrams and basins of attraction are applied to investigate the influence of initial conditions on the stable-state response of the QZS-EMEHs. The numerical outcomes illustrate that there are three main oscillation orbits for the QZS-EMEHs, and appropriate initial conditions allow the harvester to achieve large-amplitude oscillation, thus generating more electrical power. Finally, realistic ambient vibration signals are measured from a bus and a human body and subsequently applied to excite the QZS-EMEHs. The considerable output performance demonstrates the positive application prospect of QZS-EMEHs, and experimental investigations will be presented in future work.

Funding

This study was supported by the National Natural Science Foundation of China (Grant No. 12202400, 52171193), China Postdoctoral Science Foundation (2020M682336), Science and Technology Project of Henan Province (Grant No. 212102310248).

Author contribution statement

Wei Wang: Conceptualization, Methodology, Investigation, Funding acquisition, Writing – original draft. Ying Zhang: Investigation, Software, Writing – original draft. Chris R. Bowen: Writing – review & editing. Zon-Han Wei: Funding acquisition, Writing – review & editing. Junyi Cao: Writing – review & editing.

Declaration of Competing Interest

The authors declare that they have no known competing financial interests or personal relationships that could have appeared to influence the work reported in this paper.

Data availability statement

Data will be made available on reasonable request.

Reference

- 1. T. Yang, S. Zhou, S. Fang, W. Qin, D.J. Inman, Applied Physics Reviews 8, 031317 (2021).
- 2. H. Yu, N. Li, N. Zhao, Advanced Energy Materials 11, 2002646 (2021).
- 3. H. Fu, X. Mei, D. Yurchenko, S. Zhou, S. Theodossiades, K. Nakano, E.M. Yeatman, Joule 5, 1074 (2021).
- 4. H. Liang, G. Hao, O.Z. Olszewski, V. Pakrashi, International Journal of Mechanical Sciences **219**, 107130 (2022).
- 5. G. Miao, S. Fang, S. Wang, S. Zhou, Applied Energy **305**, 117838 (2022).
- 6. H. Honma, Y. Tohyama, H. Mitsuya, G. Hashiguchi, H. Fujita, H. Toshiyoshi, Journal of Micromechanics and Microengineering **31**, 125008 (2021).
- 7. M. Iqbal, M.M. Nauman, F.U. Khan, P.E. Abas, Q. Cheok, A. Iqbal, B. Aissa, International Journal of Energy Research **45**, 65 (2020).
- 8. R. Amirtharajah, A.P. Chandrakasan, IEEE journal of solid-state circuits **33**, 687 (1998).
- 9. M. El-Hami, P. Glynne-Jones, N. White, M. Hill, S. Beeby, E. James, A. Brown, J. Ross, Sensors and Actuators A: Physical **92**, 335 (2001).

- 10. S. Fang, K. Chen, J. Xing, S. Zhou, W.-H. Liao, International Journal of Mechanical Sciences **212**, 106838 (2021).
- 11. A.R.M. Siddique, S. Mahmud, B.V. Heyst, Energy Conversion and Management **106**, 728 (2015).
- 12. D.A.W. Barton, S.G. Burrow, L.R. Clare, Journal of Vibration and Acoustics **132**, 021009 (2010).
- 13. S. Zhou, J. Cao, A. Erturk, J. Lin, Applied Physics Letters **102**, 173901 (2013).
- 14. W. Deng, Y. Wang, Mechanical Systems and Signal Processing 85, 591 (2017).
- 15. W. Liu, C. Liu, B. Ren, Q. Zhu, G. Hu, W. Yang, Applied Physics Letters **109**, 043905 (2016).
- 16. F.M. Foong, C.K. Thein, B.L. Ooi, D. Yurchenko, Mechanical Systems and Signal Processing **116**, 129 (2019).
- 17. F.M. Foong, C.K. Thein, D. Yurchenko, Journal of Sound and Vibration 482, 115470 (2020).
- 18. Q. Zhang, Y. Wang, E.S. Kim, Journal of Applied Physics **115**, 064908 (2014).
- 19. M.N. Struwig, R. Wolhuter, T. Niesler, Smart Materials and Structures 27, 125007 (2018).
- 20. C.R. Saha, T. O'Donnell, N. Wang, P. McCloskey, Sensors and Actuators A: Physical **147**, 248 (2008).
- 21. B.P. Mann, N.D. Sims, Journal of Sound and Vibration 319, 515 (2009).
- 22. W. Wang, J. Cao, N. Zhang, J. Lin, W.-H. Liao, Energy Conversion and Management 132, 189 (2017).
- 23. M. Masoumi, Y. Wang, Journal of Sound and Vibration 381, 192 (2016).
- 24. B.P. Mann, B.A. Owens, Journal of Sound and Vibration **329**, 1215 (2010).
- 25. H.T. Nguyen, D. Genov, H. Bardaweel, Mechanical Systems and Signal Processing **134**, 106361 (2019).
- 26. M. Gao, Y. Wang, Y. Wang, P. Wang, Applied Energy 220, 856 (2018).
- 27. C. Liu, R. Zhao, K. Yu, H.P. Lee, B. Liao, Energy **233**, 121146 (2021).
- 28. J. Margielewicz, D. Gąska, G. Litak, P. Wolszczak, D. Yurchenko, Applied Energy 118159 (2021).
- 29. K. Wang, J. Zhou, H. Ouyang, Y. Chang, D. Xu, Mechanical Systems and Signal Processing **151**, 107368 (2021).
- 30. H. Liu, C. Hou, J. Lin, Y. Li, Q. Shi, T. Chen, L. Sun, C. Lee, Applied Physics Letters **113**, 203901 (2018).
- 31. Y. Kuang, R. Hide, M. Zhu, Applied Energy **255**, 113822 (2019).
- 32. Y. Kuang, M. Zhu, Applied Physics Letters **114**, 203903 (2019).
- 33. D.J. Inman, R.C. Singh, *Engineering vibration*. Vol. 3. 1994: Prentice Hall Englewood Cliffs, NJ.
- 34. R.L. Harne, K.-W. Wang, *Harnessing bistable structural dynamics: for vibration control, energy harvesting and sensing.* 2017: John Wiley & Sons.
- 35. R. Mickens, Journal of sound and vibration **94**, 456 (1984).